


Extremely Sharp Bending and Recoverability of Nanoscale Plates with Honeycomb Corrugation

Pengcheng Jiao,¹ Samuel M. Nicaise,² Chen Lin,² Prashant K. Purohit,² and Igor Bargatin^{2,*}

¹*Ocean College, Zhejiang University, Zhoushan 316021, Zhejiang, China*

²*Department of Mechanical Engineering and Applied Mechanics, University of Pennsylvania, Philadelphia, Pennsylvania 19104, USA*

 (Received 31 August 2018; revised manuscript received 11 January 2019; published 22 March 2019)

We investigate “sharp bending”—localized, extreme bending deformation—of corrugated nanoscale plates as well as their ability to fully recover from such bending. Unlike planar films, these mechanical metamaterials with nanoscale thickness exhibit surprising mechanical robustness and recoverability due to their periodic honeycomb corrugation and high aspect ratios (e.g., height-to-thickness ratio). An analytical model that fully characterizes one-dimensional bending of these corrugated plates at large deformations is developed and validated by comparing the predictions to experimental and finite element results. The sharp bending is enabled by a nonmonotonic moment-curvature relation that allows for the coexistence of regions of high and low curvatures despite the complete linearity of the underlying material. Systematic studies are performed to investigate the effects of the corrugation geometry parameters on the sharp bending properties, identifying the parameter space where the structures exhibit complete recovery from sharp bending. Optimized plate mechanical metamaterials could be employed for applications requiring rigid lightweight plates that can recover their shape after extreme bending deformation, for example, wings of microflyers or expandable aerospace components that need to be deployed after take off.

DOI: [10.1103/PhysRevApplied.11.034055](https://doi.org/10.1103/PhysRevApplied.11.034055)

I. INTRODUCTION

Plates that recover from extreme bending and folding deformations could allow a large structure to be stored in a small volume or recover from collisions. However, apart from a few exceptions, such as inflatable structures, solid plates or sheets do not exhibit such behavior. For example, Fig. 1(a) displays the typical crushing and releasing process for a flat sheet, such as a piece of paper or a metal foil. The sheet undergoes extreme bending deformation within narrow folds, which leads to permanent creasing after release [1,2]. The creasing damage occurs in localized, narrow regions for which the radius of curvature during bending is comparable to the thickness of the sheet. Such localized deformation often leads to strains exceeding the elastic limit, resulting in fracture or permanent plastic deformation. Some materials, such as elastomers, can recover from very large strains but are quite soft, limiting structural applications. Therefore, traditional materials either exhibit high stiffness but do not fully recover from sharp bending (i.e., are permanently damaged due to fracture or plastic flow) or exhibit sharp bending and full recovery but are not particularly stiff. A material that can do both would be highly desirable for structural applications.

For example, micro-air vehicles (MAVs or microflyers) can require the wings have high bending stiffness and low weight (e.g., wing mass is less than 5% of the total body mass) [3]. In contrast to the typical rigid composite wings of large-scale aircrafts that are not designed to change their shape, wings that can reversibly collapse can enhance the performance of MAVs [4]. Optimally, wings of MAVs should not only have high stiffness and low mass, but also be able to return to their original shape after large deformations that may result from collisions between a MAV and walls or other objects. A recent study investigated hinge-enabled wings that could recoverably “break” in order to absorb mechanical energy in an accidental collision, though the hinge component only functioned for a particular loading condition and wing geometry [5]. When considering more uniform structures or materials, this combination of high stiffness and robustness with low mass has been observed in individual carbon nanotubes [6]; however, translating the unique properties to the macroscopic scale remains a challenge.

Multiple researchers have explored the possibility of using micro- and nanostructured mechanical metamaterials to overcome this challenge [7–11]. Bulk mechanical metamaterials with a three-dimensional (3D) truss-like architecture have been studied under different extreme loading conditions, for example, compression [12–15], tension [16], and twisting [17]. With optimal design of

*bargatin@seas.upenn.edu

their micro- and nanostructures, these metamaterials could recover substantial portions of their original shapes after being deformed to strains of over 50% [18,19]. However, the previous research efforts have mostly been dedicated to mechanical metamaterials with truss-like architectures and overall cubic or similar shapes, with only a few studies focusing on plate-like geometries and their bending properties [20–22].

To address this gap, we recently introduced an alternative class of architected mechanical metamaterials with a plate geometry [23,24]. The plates featured nanoscale thickness and hexagonal corrugation as illustrated in Fig. 1(b), leading to a significantly enhanced bending stiffness and full recovery from sharp bending [Fig. 1(c)]. While our previous report [23,24] focused on the bending stiffness under small deformation (i.e., within the regime of geometric linearity), the research described here uses analytical and numerical approaches to fully investigate the large-deformation behavior, that is, sharp bending and full recovery of the nanoscale honeycomb-corrugated plates. In particular, we find that the sharp bending is enabled by

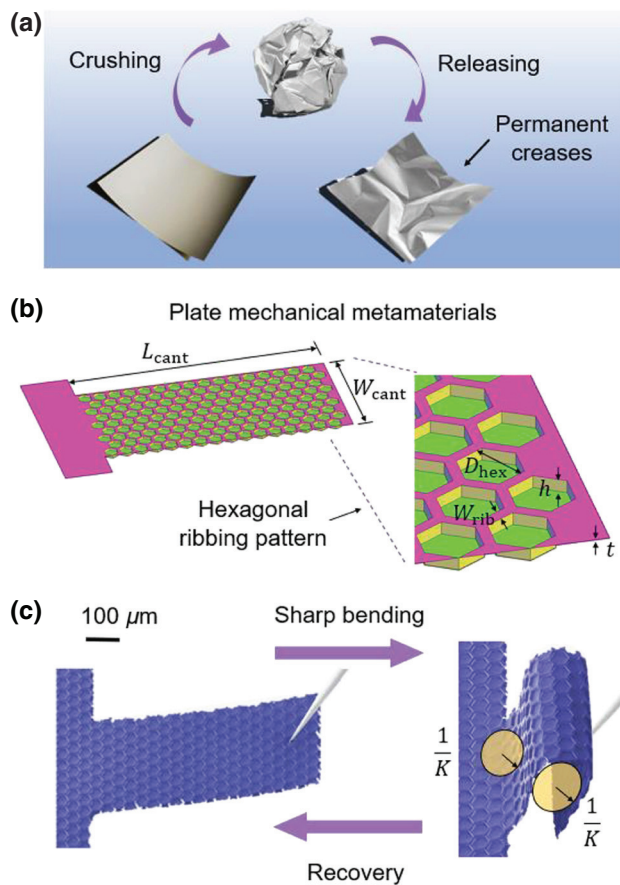


FIG. 1. (a) Crushing and releasing process for a piece of paper or metal foil leads to permanent creasing damage. (b) Plate mechanical metamaterial with hexagonal ribbing pattern. (c) Sharp bending and full recovery of the metamaterial plate.

the nonmonotonic moment-curvature relationship, which arises due to the geometric nonlinearity of the honeycomb corrugation rather than any material nonlinearity. Finally, we outline the potential applications of these robust plates to microflyer wings, energy-harvesting generators, and interstellar lightsails.

II. FABRICATION AND EXPERIMENTS

A. Fabrication process of nanoscale corrugated plates

The cantilevered honeycomb-corrugated plates used in this study are fabricated from aluminum oxide, expanding upon our previous fabrication process [23,46]. Briefly, rib patterns are etched into the surface of a silicon substrate (the mold) with photolithography and deep-reactive ion etching. Alumina is conformally deposited using atomic-layer deposition (ALD), covering the patterned mold and creating the cantilevers themselves. We laser micromachine away most of the sacrificial silicon substrate and excess alumina, leaving the desired cantilevers. Finally, we expose the samples to XeF_2 vapor in order to etch the few remaining microns of silicon and fully suspend the cantilevers.

The key characteristic of the process is that ALD is conformal, and therefore, uniform thickness can be deposited over entire nanoplates including the large face sheets and complex honeycomb ribs. The thickness of the deposited film on each silicon wafer is measured with spectral reflectometry and varies by less than approximately 0.1 nm. In high-resolution scanning-electron microscopy (SEM) images, the film is uniform and conformal throughout the structure, and no pinholes or defects are observed in any of our optical and SEM images.

B. Experimental setup and testing

As highlighted in Fig. 1(b), the main geometry parameters of the nanoplates are the plate length, plate width, film thickness, plate height, plate curvature, hexagon diameter, and rib width, which are denoted as L_{cant} , W_{cant} , t , h , K , D_{hex} , W_{rib} , respectively. These parameters are varied to determine how they influence the sharp bending and recoverability behavior. The rib widths are varied in the range of 3.3–25 μm , the hexagon minor diameter in the range of 50–200 μm , and the etch depth (or plate height) is held approximately constant at around 9–10 μm . The ALD alumina film thicknesses are 25, 40, and 50 nm. Our previous research [23] investigated a single set of geometry parameters to show only one example of sharp bending, whereas the experimental variety in this study provides for a more complete investigation. All experimental cantilevers have constant dimensions of 0.5 mm width and 1 mm length.

Experimental testing is carried out using a micromanipulator probe, as shown in Fig. 2(a), with simultaneous

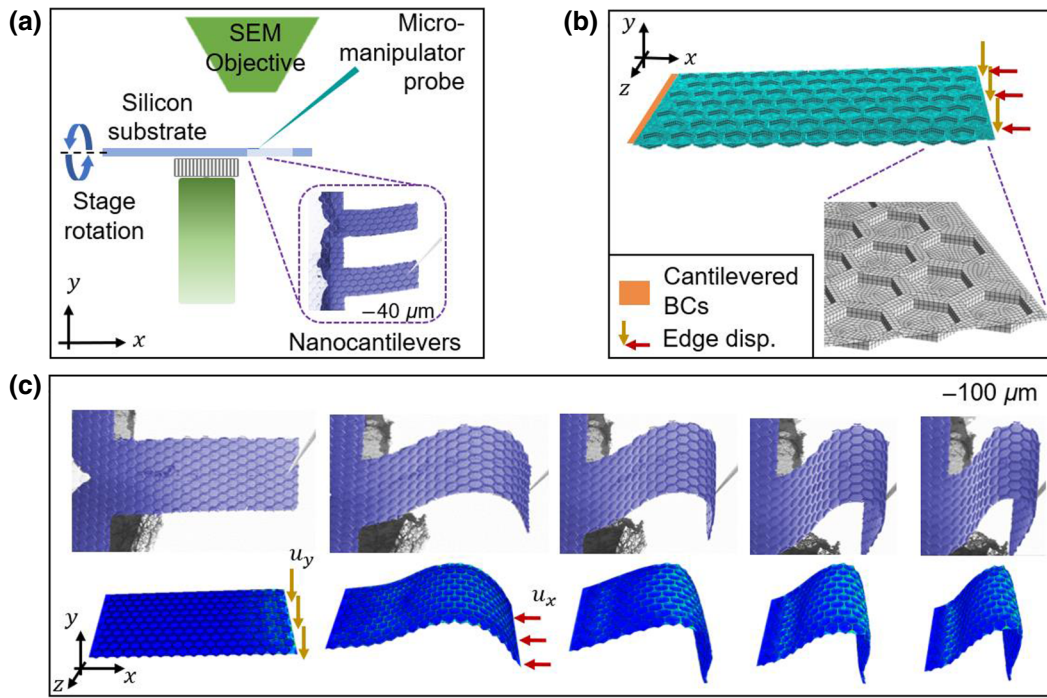


FIG. 2. (a) Experimental set up for the bending of honeycomb nanocantilevers. (b) FE modeling of the nanocantilevers. (c) Comparison of the deflection configurations between the experimental observations and numerical predictions for a cantilever ($L_{\text{cant}} = 1 \text{ mm}$, $W_{\text{cant}} = 0.5 \text{ mm}$, $D_{\text{hex}} = 50 \mu\text{m}$, $W_{\text{rib}} = 10 \mu\text{m}$, and $t = 25 \text{ nm}$).

recording of the deformed shapes of the bent cantilever [46]. This setup allows us to control the displacement of the cantilever as well as capture *in situ* high-resolution images of the resulting bending and deflection. Samples are adhered to the movable SEM stage and positioned with respect to the nanomanipulator probe such that the tip of the probe and the tip of the cantilever are just barely in contact. Cantilever deflection proceeds by bending the cantilever tip downward [y in Fig. 2(a)], axially compressing the cantilever [x in Fig. 2(a)] to induce sharp bending until the tip and base of the cantilever are almost touching, and then unloading the displacement to let the cantilever return to the original position. During this process, we record sequences of SEM micrographs. In most cases, each cantilever is bent in the same sequence two or three times to see if there are any obvious permanent deformation-induced shape changes between cycles or variations in the final unloaded position.

III. SIMULATION AND DISCUSSION

A. Finite element (FE) model

Next, we determine how well the experimentally observed deformation could be predicted by finite element (FE) models with purely elastic material behavior of alumina using Abaqus R2017x [see Fig. 2(b)]. To simulate the buckling-induced sharp bending, the FE analysis is

carried out in two steps. First, displacement in the y direction u_y is simulated using the dynamic/explicit solver with consideration of geometric nonlinearity (i.e., Nlgeom) to introduce structural asymmetry, and then displacement in the x direction u_x is simulated using the dynamic/explicit solver Nlgeom to obtain the sharply bent configurations with large deformation [25]. These simulation steps match the boundary conditions applied in the experiments, where a prescribed tip-displacement is applied to a specific portion of the nanocantilever. Figure 2(b) displays the boundary and loading conditions of the nanocantilevers. The model is clamped at one end and is free to move at the other end. The element size and type, the material properties, and loading conditions are detailed in Appendix A. The displacements in the u_y and u_x directions are 0.05 and 0.7 mm, respectively. As shown in Fig. 2(c), there is excellent agreement between experimental and numerical deformation profiles throughout the loading and unloading processes (see Appendix H for more details).

B. Large deformation of corrugated nanocantilevers

This agreement allows us to use the predictions of the FE model to develop an analytical description of large bending deformations for the architected plates with nanometer thickness. For small deformations, the moment is the product of the curvature and bending stiffness. However, at large deformations, the relationship becomes nonlinear and

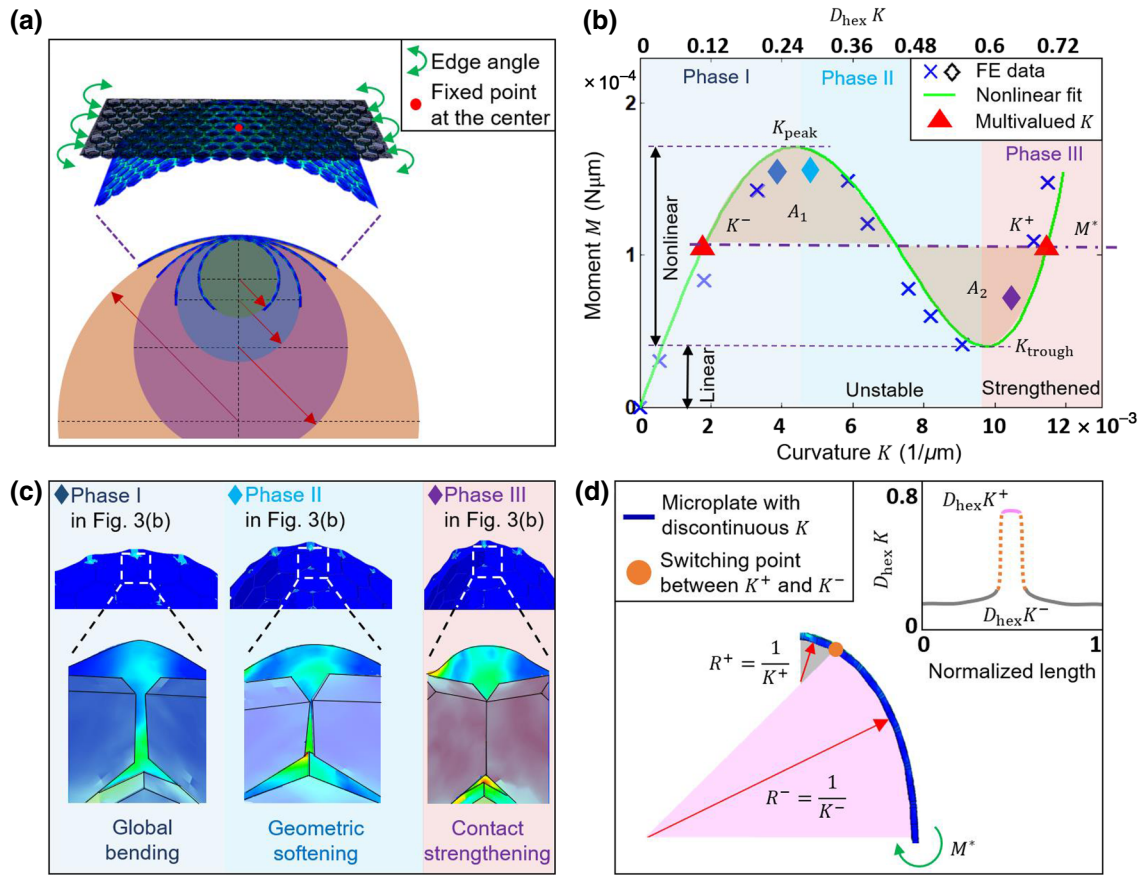


FIG. 3. (a) FE modeling of the nanocantilevers subjected to edge angle at the two ends. (b) FE data and nonlinearly fitted results of the moment-curvature relationship ($D_{\text{hex}} = 60 \mu\text{m}$, $W_{\text{rib}} = 12 \mu\text{m}$ and $t = 25 \text{nm}$). (c) Phase transition of the nanocantilevers due to the geometrical nonlinearity caused by the buckling of the ribs and sidewalls (the insets zoom in on the deformation of ribs). In phase I, the ribs are elastically deflected. In phase II, the ribs exhibit softening nonlinearity as the sidewalls do not contact each other. In phase III, the sidewalls start contacting, leading to stiffening nonlinearity. (d) Comparison of the shape changes from continuous curvature to discontinuous curvature, that is, R^- and R^+ , under the edge moment M^* illustrated in Fig. 3(b).

even multivalued (i.e., one moment may correspond to different curvatures). To quantify this nonlinear relationship between the moment and curvature, various curvatures are applied in the FE model by prescribing edge angles at the two ends and fixing the center point, as shown in Fig. 3(a). The modeled cantilevers deform as pure cylinders, and we use the Canny edge algorithm [26] to accurately capture the corresponding radii of curvature. Figure 3(b) shows the FE moment vs curvature data and the fitted nonlinear curve. Note that the material behavior of the plates remains linear elastic, and the nonmonotonic moment-curvature relationship is solely due to the geometric nonlinearity caused by the honeycomb structure under large bending deformations.

As shown in Figs. 3(b) and 3(c), the mechanical response of the plates can be divided into three phases: global bending (I), geometric softening (II), and contact strengthening (III). In phase I, the plates start with a linear elastic response and gradually transition to nonlinear elastic as the rotation angle increased. The curvature

corresponding to the peak moment, $K_{\text{peak}} \approx (3.5D_{\text{hex}})^{-1}$, serves as the boundary between phases I and II. In phase II (softening), the moment-curvature curve has a negative slope and becomes unstable, making it unobservable in experiments. The downward slope of the moment-curvature response in this phase is due to the buckling of the ribs. The curvature corresponding to the trough moment $K_{\text{trough}} \approx (1.9D_{\text{hex}})^{-1}$, serves as the boundary between phases II and III. In phase III (contact strengthening), the sidewalls start contacting one another, resulting in a positive slope and stable moment-curvature curve.

C. Nonmonotonic moment-curvature response

Nonlinearly fitting the FE modeling data, the moment-curvature relationship of the sharply bent nanocantilevers is best described by [46]

$$M = DK(1 - 0.37D_{\text{hex}}K - 7.23D_{\text{hex}}^2K^2 + 8.82D_{\text{hex}}^3K^3), \quad (1)$$

where M and K are the moment and curvature, respectively, D is the small-deformation bending stiffness, and the higher-order terms of K determine the geometric nonlinearity and instability of large bending deformations [27,28].

When moments are applied to the two free ends of the plates within the nonlinear region, for example M^* in Fig. 3(b), there are two stable curvatures corresponding to each moment. Accordingly, the curvature of the sharply bent plates becomes discontinuous in FE simulations, as shown in Fig. 3(d). The maximum and minimum radii R^+ and R^- , respectively, match the fitted curvatures K^+ and K^- that are obtained based on the moment M^* at the Maxwell line [29]. Given the up-down-up shape of the moment-curvature relations, we define the Maxwell line (M^*) between the moments at K_{peak} and K_{trough} such that the area under the moment-curvature curve above the line is the same as the area below the line, that is, $A_1 = A_2$. Therefore, we obtain K^+ and K^- that correspond to the moment M^* at the Maxwell line. The Maxwell line is a graphical way of ensuring that the coexisting phases have the same Gibbs free energy per unit mass (or the same potential energy if entropy does not play an important role). This has previously been used to model the coexistence of phases for neck propagation in polymers and metals [30], bulge propagation in balloons [31], and wrinkle-ridge transitions in thin film-substrate systems [32]. A metallic alloy that had nonlinear moment-curvature behavior under a pure bending load was also reported in the literature [33].

Note that the overall up-down-up shape of the moment-curvature curve [Fig. 3(b)] has been previously theoretically analyzed in the literature for reversible postbuckling of elastic rods [29,34]. Nonmonotonic moment-curvature curves have also been experimentally reported for individual nanotubes [35] and NiTi tubes [36]. In particular, when the NiTi tubes are bent, the upper half in tension shows nanoscale material changes due to phase transitions, but the lower half in compression does not. Ultimately, the nonlinear moment-curvature relation of these bent NiTi tubes inherits its nonmonotonic character from the nonlinear tensile response of the NiTi material. In contrast, the origins of the nonmonotonic moment-curvature relation in our corrugated plates has to do with its corrugated geometry and the resulting geometric nonlinearity rather than the material behavior.

By varying the honeycomb geometry parameters of the FE models, the linear bending stiffness is determined to be

$$D = \frac{Et^3}{12(1-\nu^2)} \left(\frac{D_{\text{hex}}}{W_{\text{rib}}} + 1 \right)^2, \quad (2)$$

which is consistent with our previous results on small-deformation bending [23]. Since the bending stiffness scales cubically with thickness while body forces due

to gravity scale linearly, extremely thin plates can bend under gravity. This linear stiffness can be used to estimate the straightness (i.e., tip deflection-to-length ratio) of the plates due to gravity (see Appendix B)

$$\frac{\Delta y_{\text{max}}}{L_{\text{cant}}} = \frac{L_{\text{cant}}^3}{t^2} \times \frac{3(1-\nu^2)\rho g}{2E} \times \frac{W_{\text{rib}}^2 [(D_{\text{hex}} + W_{\text{rib}})^2 + 4hD_{\text{hex}}]}{(D_{\text{hex}} + W_{\text{rib}})^4}, \quad (3)$$

where Δy_{max} , ρ , g , and t_{min} refer to the deflection at the cantilever tip, density of alumina, gravitational constant, and minimum thickness that keeps the plates straight, respectively. For the minimum thickness, $t_{\text{min}}^{\text{exp}} = 25$ nm is used in our experiments and the displacement due to gravity is approximately two-orders of magnitude smaller than the cantilever length. Therefore, the displacement is negligible in the sharp bending experiments since the total displacement is comparable to the cantilever length.

IV. THEORETICAL MODELING

A. Governing equation

After determining the fundamental relationship between the moment and curvature, we develop an analytical model using the Cosserat rod theory [37]. The governing equation for describing the theoretical deflection is derived as (see Appendix C)

$$D \frac{d^2\theta}{ds^2} \left[1 - 0.74D_{\text{hex}} \frac{d\theta}{ds} - 21.69D_{\text{hex}}^2 \left(\frac{d\theta}{ds} \right)^2 + 35.28D_{\text{hex}}^3 \left(\frac{d\theta}{ds} \right)^3 \right] + \cos(\theta)N_y - \sin(\theta)N_x = 0, \quad (4)$$

where θ , N_x , and N_y are the rotation angle, and the longitudinal and transverse components of the constant external forces N that act on the free end of the cantilever, respectively. The boundary conditions are given as: $\theta|_{s=0} = \theta'|_{s=L} = 0$. Note that the plates could buckle when they reach the peak moment, in which case there would no longer be a unique solution, since large moments or forces could correspond to two distinct curvatures [one in each upward sloping branch of the moment-curvature relations, as shown in Fig. 3(b)]. In addition, the body forces of the nanocantilevers are neglected because of their extremely low self weight. However, they could also be included in the equation if necessary.

B. Theoretical results and comparison

Figure 4 compares the deflection configurations of select nanocantilevers, showing that the theoretical results, FE model predictions, and experimental observations are in good agreement (see Appendix D). To reveal the effect of the hexagonal geometry parameters on the mechanical

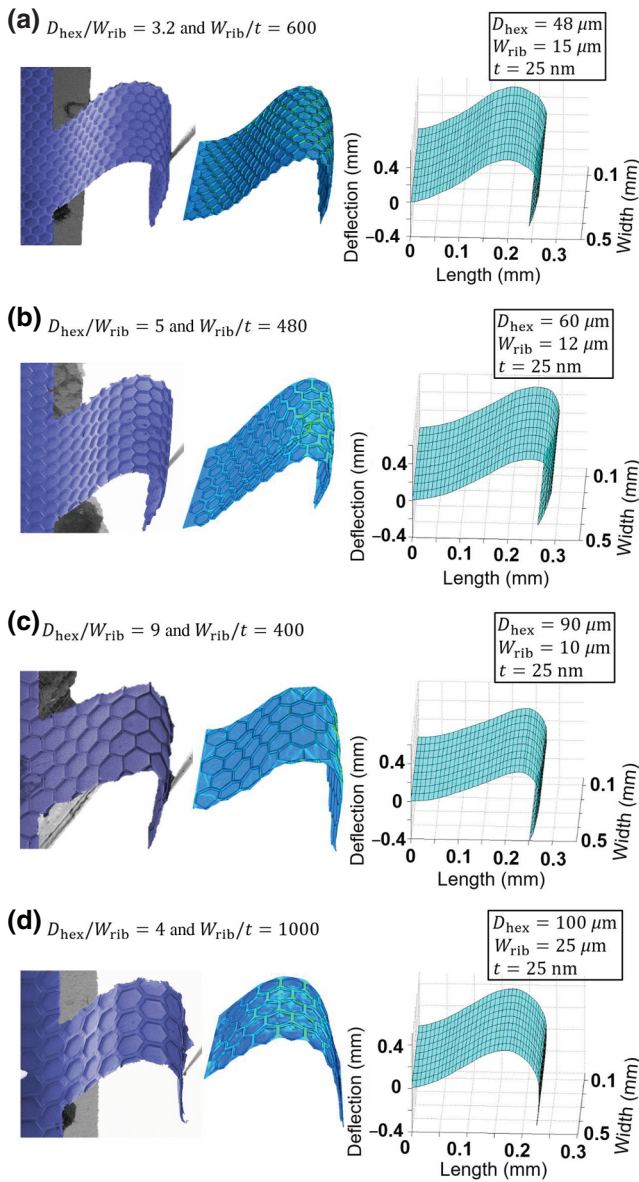


FIG. 4. Examples of the deflection configurations comparing the experimental (left), numerical (middle), and theoretical (right) results with respect to the ratios of hexagonal diameter-to-rib width and rib width-to-film thickness for (a) $D_{\text{hex}} = 48 \mu\text{m}$ and $W_{\text{rib}} = 15 \mu\text{m}$, (b) $D_{\text{hex}} = 60 \mu\text{m}$ and $W_{\text{rib}} = 12 \mu\text{m}$, (c) $D_{\text{hex}} = 90 \mu\text{m}$ and $W_{\text{rib}} = 10 \mu\text{m}$, and (d) $D_{\text{hex}} = 100 \mu\text{m}$ and $W_{\text{rib}} = 25 \mu\text{m}$ ($t = 25 \text{ nm}$ for all cases).

response, that is, sharp bending and recovery, the hexagonal diameter D_{hex} , rib width W_{rib} , and thickness t are varied. Specifically, the sharp bending and shape recovery are investigated with respect to the ratios of diameter to rib width, $D_{\text{hex}}/W_{\text{rib}}$, and rib width to thickness, W_{rib}/t , as discussed below.

According to Fig. 1(c) and other experimental results, the sharpest bending we observe corresponds to a radius of curvature of approximately two hexagonal cells'

diameters, which usually occurs at the base and the middle of the cantilever. Thus, we consider the plate to be sharply bent when the curvature is $K \geq (2D_{\text{hex}})^{-1}$, and thus the limit of the sharp bending ratio is defined as: $R_{\text{SB}} = (D_{\text{hex}}K)^{-1} \geq 2$. The recovery, on the other hand, is determined by the maximum principal strains. In experiments, a plate-like structure is likely to recover its original shape when the critical strains are below the fracture strain, which scales as $t^{-1/2}$, and varies between 0.8% and 1.5% for film thicknesses between 25 and 100 nm [38]. Based on the analysis of the FE and experimental comparison, we find that sharp bending occurs when $300 < W_{\text{rib}}/t < 800$ [see, for example, Figs. 4(a)–4(c)]. Nonrecoverable deformations (i.e., permanent cracks) occur when the diameter-to-rib width is $D_{\text{hex}}/W_{\text{rib}} > 7$, for example, Fig. 4(c). Since fewer hexagonal walls exist when the diameter is large, the stresses are more concentrated, resulting in local fracture.

V. RESULTS AND DISCUSSION

A. Sharp bending and recovery of the nanoplates

To fully explore the sharp bending and shape recovery behaviors of the plate mechanical metamaterials, we numerically investigate the sharp bending ratio R_{SB} and maximum strain with respect to $D_{\text{hex}}/W_{\text{rib}}$ and W_{rib}/t (see Appendix E). Figure 5(a) shows the density plot of the sharp bending ratio, where $D_{\text{hex}}/W_{\text{rib}}$ and W_{rib}/t are varied from 3 to 13 and 50 to 1100, respectively. The cantilevers generally exhibit sharp bending when they are relatively thin (specifically, $W_{\text{rib}}/t > 300$). Figure 5(b) displays the distribution of the maximum strains for $D_{\text{hex}}/W_{\text{rib}}$ and W_{rib}/t in the same ranges. Given the thicknesses fabricated and tested (i.e., 25, 40, and 50 nm), 0.8%, 1.2%, and 1.5% are used as the limit states for full recovery [39]. By combining the obtained limit states for sharp bending (R_{SB}) and recovery (maximum strain), Fig. 5(c) highlights the overlapping region that provides the geometric parameters necessary for the recoverable sharp bending. It can be seen that the targeted geometries are approximately $3 < D_{\text{hex}}/W_{\text{rib}} < 10$ and $800 > W_{\text{rib}}/t > 300$. This FE prediction accurately matches our experimental observations.

B. Other corrugation patterns

In addition to the honeycomb plates, we consider other regular corrugation patterns. To achieve the corrugation patterns, we define two design criteria: (1) the no-straight-line rule (i.e., no straight lines can go through the corrugated plates without contacting side-walls); and (2) The regularity rule (i.e., uniform pattern cells are separated by a uniform gap) (see Appendix F). Using the design criteria, two patterns are obtained, including rhombille and basketweave plates. Both of

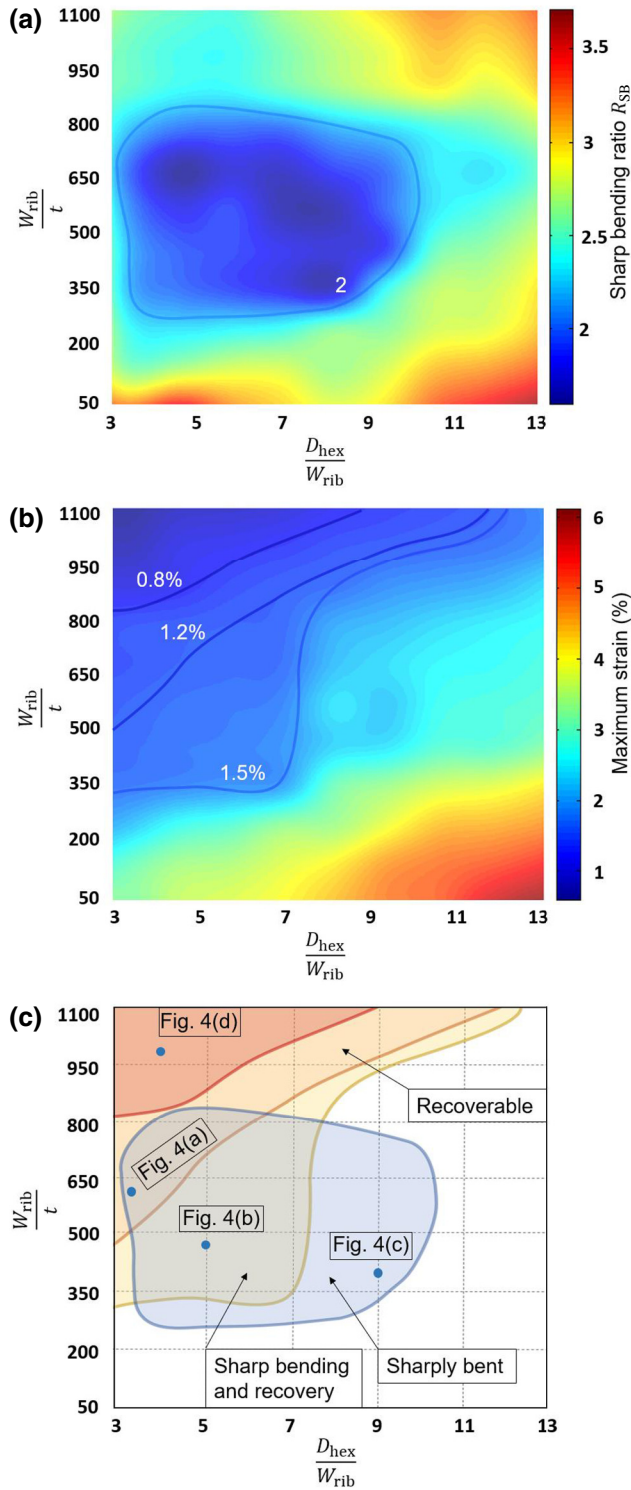


FIG. 5. Density plots of the (a) sharp bending ratio $R_{SB} = (KD_{hex})^{-1}$ and (b) maximum principal strains with respect to D_{hex}/W_{rib} and W_{rib}/t . (c) Targeted geometric ratios that provide recoverable sharp bending for the nanocantilevers.

these show nonmonotonic moment-curvature curves in FE simulations. However, the hexagonal pattern offers the best performance with the largest overlapping area

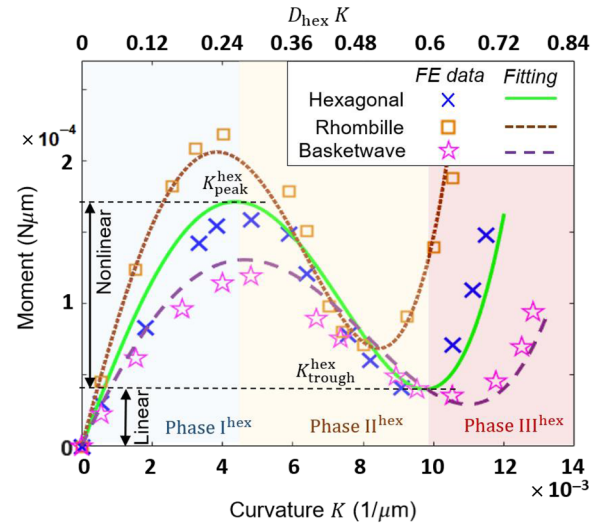


FIG. 6. Comparison of the nonmonotonic moment-curvature relationships for the nanocantilevers with corrugated, rhombille, and basketweave patterns ($D_{hex} = D_{rohm} = D_{bask} = 60 \mu\text{m}$, $W_{rib} = W_{rohm} = W_{bask} = 12 \mu\text{m}$, $t = 25 \text{ nm}$, and $h = 10 \mu\text{m}$).

(see Appendix G). Figure 6 presents the comparison of the moment-curvature relationships between the hexagonal [Fig. 3(b)], rhombille, and basketweave nanocantilevers with similar parameters: $D_{hex} = D_{rohm} = D_{bask} = 60 \mu\text{m}$, $W_{rib} = W_{rohm} = W_{bask} = 12 \mu\text{m}$, $t = 25 \text{ nm}$, and $h = 10 \mu\text{m}$, respectively.

Nonmonotonic $M - K$ curves with three phases (i.e., phase I: global bending, phase II: geometric softening, and phase III: contact strengthening) are obtained from all the patterns. Compared with the hexagonal and basketweave patterns, the phase transition curvatures of the rhombille nanocantilevers (i.e., K_{peak}^{rhom} and K_{trough}^{rhom}) are the lowest, while the corresponding moments resulting in those curvatures are the highest. Because the space between ribs in the rhombille pattern [i.e., the darker areas in Fig. 13(a)] tend to be smaller than that of the corrugated and basketweave patterns, the vertical webbings of the rhombille nanocantilevers first contact one another. Therefore, the transition limits of curvatures (i.e., K_{peak}^{rhom} and K_{trough}^{rhom}) are the lowest for the rhombille nanocantilevers. In contrast, the spaces between ribs for the basketweave pattern are larger than those for the rhombille and corrugated plates, and the corresponding phase transition limits of curvatures are the largest, as shown in Fig. 13(b).

C. Scaling of the corrugated nanoplates

We also note that, in principle, recoverable sharp bending can be realized at the macroscale as long as the structures have the same aspect ratios. However, body weight tends to play a much bigger role at the macroscale, limiting the size of the structures that can exhibit this behavior. The experimental nanocantilevers have extremely large aspect

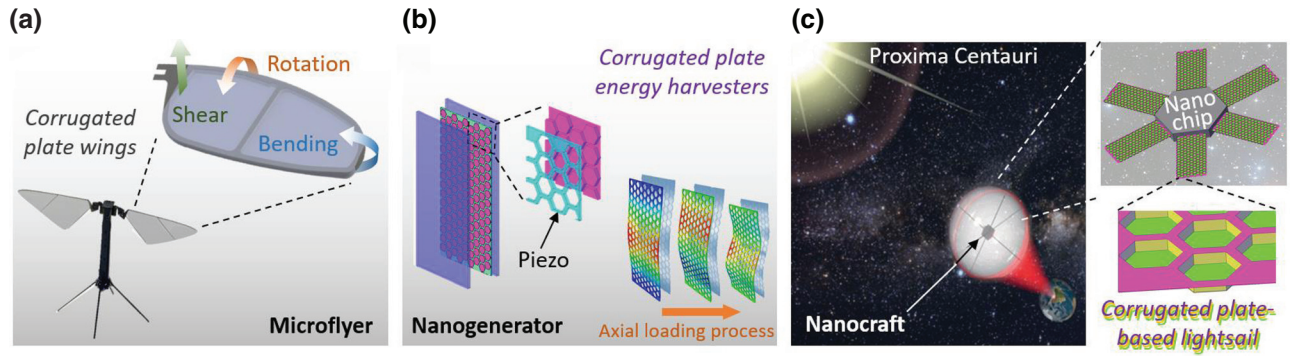


FIG. 7. Potential applications of the ultralight, high-stiffness corrugated nanoplates with full deformation recovery in (a) microflyers [40], (b) nanogenerators [43,44], and (c) spacecraft [45].

ratios (i.e., height-to-thickness ratio is approximately 10^3). Similar nonmonotonic moment-curvature relationships are obtained from the numerical simulations for the corrugated nanocantilevers with mm-scale thickness as long as we neglect the gravity body forces. However, in practice, structures with such large height-to-thickness aspect ratios would suffer from bending due to gravity. According to Eq. (3), the maximum deflection Δy_{\max} scales quadratically (rather than linearly) with cantilever length. However, the minimum thickness t_{\min} needed to neglect the body forces in Eq. (B15) scales as approximately $L^{3/2}$ rather than L^2 , which is inconsistent with scaling all dimensions by the same factor. In other words, the cantilever length L increases the body force-induced deflection y_{\max} more quickly than the respective minimum thickness t_{\min} needed to maintain a straight structure. Therefore, the body weight will become increasingly important when the cantilevers are scaled up to the millimeter scale.

D. Potential applications and impact

Figure 7 illustrates the potential applications of the reported hexagonal corrugated nanocantilevers. Figure 7(a) shows how the corrugated plates can be used as collapsible flapping wings for microflyers [40]. Since many hover-capable microflyers are based on the evolution of insect flight in nature, microwings are typically designed for collapsible flapping in a nearly horizontal plane [41]. Consequently, the microwings should not only have high stiffness and low mass, but also high robustness such that they can fully recover from large deformations resulting from collisions. The sharp bending recovery process of the corrugated plates provides a mechanism to dissipate energy and recover the original shape, thus protecting microflyers from accidental collisions. In addition, the corrugated nanoplates can be designed as active or semi-active microwings that change shape configurations for different purposes (e.g., accelerating, escaping, steering, or landing) [42]. For example, previously reported hinge-enabled microwings provided sharp bending performance

in microrobots to reduce body rotation and dampen energy from accidental collision [5].

Figure 7(b) illustrates the potential application of corrugated plates as nanogenerators in energy harvesting. Piezoelectric material is placed between the hexagonal cells, and the piezo-composite corrugated plates are constrained between two rigid walls [43]. Under axial compression, the biwalled piezo-plates are postbuckled, which results in large deformations to the piezoelectric material and hence generates electrical power [44]. Since the postbuckling behavior can be controlled through pattern design, the power generated by the piezo-plates could be optimized for nanogenerators in specific applications.

Finally, Figure 7(c) illustrates an application of plate mechanical metamaterials in space travel. We envision that the controllable mechanical behavior could be useful for lightsails [45]. For example, full recovery after nearly 100% strain means that the corrugated plate-based lightsails with nanoscale thickness can be rolled or folded to reduce the overall size during launch and then deployed to cover many square meters in area for maximum thrust.

VI. CONCLUSIONS

In this paper, we report and characterize the recoverable sharp bending of ultrathin cantilevers with honeycomb corrugation. Cantilevered plates are fabricated and experimentally tested to determine the configurations of large bending deformations. To determine the influence of hexagonal corrugation pattern on the recoverably sharp bending, numerical and theoretical models are developed. The designed hexagonal corrugation with high aspect ratios (e.g., height-to-thickness ratio) leads to the surprising mechanical robustness and recoverability of the nanocantilevers. Parametric studies are carried out to quantitatively investigate the effect of the corrugated cells on sharp bending and recovery with respect to the ratios of diameter-to-rib width and rib width-to-thickness. The findings provide a fundamental understanding of large bending

deformation in plate mechanical metamaterials, which suggest that the plates are promising for applications that require both high bending stiffness and full recovery, such as wings of microflyers or aerospace components.

ACKNOWLEDGMENT

P.J. acknowledges the Startup Fund of the Hundred Talent Program at the Zhejiang University. P.K.P. acknowledges support through a National Science Foundation Grant No. NSF CMMI 1662101. This work was carried out in part at the Singh Center for Nanotechnology, which is supported by the NSF National Nanotechnology Coordinated Infrastructure Program under Grant No. NNCI-1542153.

P.J. and S.M.N. contributed equally to the paper.

APPENDIX A: DETAILS IN THE FE MODELS

In order to capture the deformation of the hexagonal ribs (i.e., ensure that ribs have the freedom to deform), the size of the shell elements (S4R) is chosen as $1/3$ of the rib width W_{rib} [46]. The geometric properties, element size, and solving algorithm of the FE models are summarized in Table I.

APPENDIX B: MINIMUM THICKNESS THAT MAINTAINS STRAIGHT NANOCANTILEVERS

To theoretically obtain the minimum thickness t that keeps the nanocantilevers straight, it is necessary to take into account the body weight of the structures, because the straightness of the corrugated nanocantilevers is affected by gravity. Figure 8(a) illustrates the deformation of a nanocantilever with the body weight $BW(x)$. To formulate the problem, it is converted into a weightless nanocantilever subjected to the distributed load $Q(x)$, where $Q = BW$ as shown in Fig. 8(b).

To determine the distributed load $Q(x)$ [i.e., the body weight $BW(x)$], it is necessary to obtain the volume of the

TABLE I. Geometric and material properties, element, and loading conditions.

Geometric properties	Length L_{cant} (mm)	1
	Width W_{cant} (mm)	0.5
	Thickness t (nm)	25
	Rib width W_{rib} (μm)	10
	Hex. diameter D_{hex} (μm)	50
	Material properties	Young's modulus (GPa)
Poisson's ratio		0.22
Density ($\times 10^{-9}$ ton/ mm^3)		3.95
Element Size and Type	Size	$\frac{1}{3}W_{\text{rib}}$
	Type	S4R
Loading in Displacement	Bending	$\frac{1}{10}W_{\text{cant}}$
	Compression	$\frac{1}{10}L_{\text{cant}}$

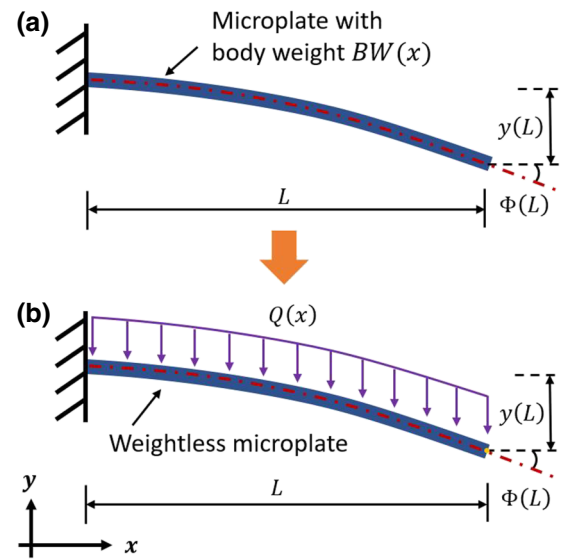


FIG. 8. Illustrations of (a) a straight nanocantilever that has the body weight $BW(x)$, and (b) deflection of a weightless nanocantilever subjected to the distributed load $Q(x)$ ($Q = BW$).

structures. Note that the honeycomb nanocantilevers consist of two parts, including the face sheets and sidewalls. The volume of the face sheets is given as

$$V_{\text{FS}} = LWt, \quad (\text{B1})$$

where L , W , and t denote the length, width, and thickness of the corrugated cantilevers, respectively. The sidewalls are affected by the number of the hexagons. Therefore, the volume of the sidewalls can be written as

$$V_{\text{sw}} = 2\sqrt{3} \cdot N_{\text{num}} \cdot thD_{\text{hex}}, \quad (\text{B2})$$

where h and D_{hex} are the height and hexagonal diameter of the nanocantilevers. N_{hex} is the total number of the hexagon corrugations, which is given as

$$N_{\text{num}} = N_L \cdot N_w = \frac{2\sqrt{3}}{3} \frac{WL}{(D_{\text{hex}} + W_{\text{rib}})^2}. \quad (\text{B3})$$

Putting Eq. (B3) into Eq. (B2), the volume of the sidewalls yields

$$V_{\text{sw}} = 4 \frac{LWthD_{\text{hex}}}{(D_{\text{hex}} + W_{\text{rib}})^2}, \quad (\text{B4})$$

and thus, the total volume of the nanocantilevers is obtained as

$$V = V_{\text{FS}} + V_{\text{sw}} = LWt \left[4 \frac{hD_{\text{hex}}}{(D_{\text{hex}} + W_{\text{rib}})^2} + 1 \right]. \quad (\text{B5})$$

Therefore, the unit distributed load \bar{Q} is

$$\bar{Q} = \rho g \bar{V} = \rho g t \left[4 \frac{h D_{\text{hex}}}{(D_{\text{hex}} + W_{\text{rib}})^2} + 1 \right]. \quad (\text{B6})$$

where ρ , g and \bar{V} refer to the density of the nanocantilevers (i.e., alumina), gravitational constant, and unit volume.

Next, let us determine the bending deflection of the cantilever caused by \bar{Q} . It is worth pointing out that the nanocantilevers are subjected to extremely large deformations (i.e., sharp bending) in this study; however, by only considering the unit distributed load \bar{Q} , it is sufficient to assume the deflection of the cantilever is a small deformation. Consequently, the moment-curvature relationship [Eq. (1)] is reduced to

$$M = DK. \quad (\text{B7})$$

K denotes the curvature of the nanostructures, which can be simplified as

$$K = \frac{d^2 y(x)}{dx^2}, \quad (\text{B8})$$

where $y(x)$ is the transverse deflection caused by the unit distributed load (i.e., the body weight). Therefore, the deflection of the weightless, cantilevered nanocantilevers subjected to \bar{Q} can be written as

$$y(x) = \frac{\bar{Q} L^4}{24D} \left(\frac{x}{L} \right)^2 \left[\left(\frac{x}{L} \right)^2 - \frac{4x}{L} + 6 \right], \quad (\text{B9})$$

where the effective bending stiffness is given as [Eq. (2)]

$$D = \frac{Et^3}{12(1-v^2)} \left(\frac{D_{\text{hex}}}{W_{\text{rib}}} + 1 \right)^2. \quad (\text{B10})$$

Inserting Eq. (B10) into Eq. (B9) and letting $x = L$, the maximum body weight-induced deflection is

$$y_{\text{max}} = y|_{x=L} = \frac{3(1-v^2)\bar{Q}L^4}{2Et^3} \left(\frac{D_{\text{hex}}}{W_{\text{rib}}} + 1 \right)^{-2}. \quad (\text{B11})$$

Further substituting Eq. (B6) into Eq. (B11), we obtain

$$y_{\text{max}} = y|_{x=L} = \frac{3(1-v^2)\rho g L^4}{2Et^2} \frac{W_{\text{rib}}^2}{(D_{\text{hex}} + W_{\text{rib}})^4} \times [(D_{\text{hex}} + W_{\text{rib}})^2 + 4hD_{\text{hex}}], \quad (\text{B12})$$

which leads to

$$t = \frac{L^2}{\left(\frac{D_{\text{hex}}}{W_{\text{rib}}} + 1 \right)^2} \times \sqrt{\frac{3(1-v^2)\rho g}{2Ey_{\text{max}}} \left[\left(\frac{D_{\text{hex}}}{W_{\text{rib}}} + 1 \right)^2 + 4 \frac{hD_{\text{hex}}}{W_{\text{rib}}^2} \right]}. \quad (\text{B13})$$

Note that y_{max} can be used to identify the straightness of the nanocantilevers. We define the straightness of the nanocantilevers with respect to the cantilever length L as

$$y_{\text{max}} \leq \zeta L, \quad (\text{B14})$$

where $\zeta \ll 1$ is the straightness factor.

Substituting Eq. (B14) into Eq. (B13), the minimum thickness that keeps the corrugated nanocantilevers straight is eventually obtained as

$$t_{\text{min}} = \frac{L^{3/2}}{\left(\frac{D_{\text{hex}}}{W_{\text{rib}}} + 1 \right)^2} \times \sqrt{\frac{3(1-v^2)\rho g}{2E\zeta} \left[\left(\frac{D_{\text{hex}}}{W_{\text{rib}}} + 1 \right)^2 + 4 \frac{hD_{\text{hex}}}{W_{\text{rib}}^2} \right]}. \quad (\text{B15})$$

For example, the minimum thickness that keeps the nanocantilever in Fig. 3 straight is obtained as $t_{\text{min}} = 15.4$ nm, when $D_{\text{hex}} = 60$ μm , $W_{\text{rib}} = 12$ μm , $h = 10$ μm , $L = 1$ mm, and $\zeta = 0.07$. Therefore, the thickness of the nanocantilevers in Fig. 3 ($t = 25$ nm) satisfies the straightness criterion. In fact, cantilevers with lengths of up to several mm would also exhibit negligible bending due to gravity. Coincidentally, $t_{\text{min}} = 15.4$ nm is also comparable to our experimental estimation: $t_{\text{min}}^{\text{exp}} \approx 15$ nm, which is due to fabrication-related stress gradients rather than gravity.

APPENDIX C: THEORETICAL MODELING

Figure 9 is a model for the deformation shape of the nanocantilevers subjected to tip forces in the longitudinal and transverse directions N_x and N_y . The force can be expressed as

$$N = N_x \hat{e}_x + N_y \hat{e}_y, \quad (\text{C1})$$

where \hat{e}_x and \hat{e}_y are the unit vectors in the lab coordinates, and N_x and N_y are constants [i.e., $(d/ds)N_x = (d/ds)N_y = 0$]. Therefore, we have the relationship between the rotation angle of the cantilever $\theta(s)$ and the displacements in

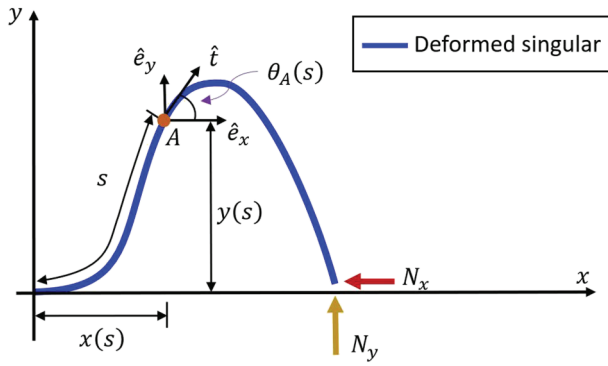


FIG. 9. Model of a largely deformed nanocantilever subjected to quasistatic forces in the longitudinal and transverse directions.

the x and y directions $x(s)$ and $y(s)$ as

$$\begin{cases} \frac{dx(s)}{ds} = \cos \theta \\ \frac{dy(s)}{ds} = \sin \theta \end{cases} \quad (\text{C2})$$

According to the Cosserat rod theory [37], the governing equation of deflected nanocantilevers is given as

$$\frac{dM}{ds} + \lambda \hat{t} \times N = 0, \quad (\text{C3})$$

where

$$\hat{t} = [\cos(\theta)\hat{e}_x + \sin(\theta)\hat{e}_y]. \quad (\text{C4})$$

The stretching is

$$\lambda = 1 + \frac{N_x}{A_{xx}}. \quad (\text{C5})$$

Note that A_{xx} , the extensional stiffness of the nanocantilevers, can be written as

$$A_{xx} = \frac{\bar{E} \cdot \bar{A}}{TC_{EF}} = \frac{\bar{E}bt}{TC_{EF}}, \quad (\text{C6})$$

where $\bar{E} \cdot \bar{A}$ and TC_{EF} are the extensional stiffness of the nanocantilevers and the tensile-compressive enhancement factor of the nanocantilevers, respectively.

We assume that the nanocantilevers are inextensible and hence $\lambda = 1$, thus the governing equation can be expressed as

$$\frac{dM}{ds} + \cos(\theta)N_y - \sin(\theta)N_x = 0. \quad (\text{C7})$$

We have the relationship between the rotation of the neutral axis and the curvature as

$$K = \theta'(s). \quad (\text{C8})$$

Putting Eqs. (C1) and (C8) into Eq. (C7), the governing equation for the nanocantilever is obtained as

$$D \frac{d^2\theta}{ds^2} \left[1 - 0.74D_{\text{hex}} \frac{d\theta}{ds} - 21.69D_{\text{hex}}^2 \left(\frac{d\theta}{ds} \right)^2 + 35.28D_{\text{hex}}^3 \left(\frac{d\theta}{ds} \right)^3 \right] + \cos(\theta)N_y - \sin(\theta)N_x = 0, \quad (\text{C9})$$

where the bending stiffness D is given in Eq. (2).

Note that Eq. (C9) can be converted into two first-order differential equations as

$$\begin{cases} X_2 = X_1' \\ X_1' = \frac{X_2}{D(1 - 0.74D_{\text{hex}}X_2 - 21.69D_{\text{hex}}^2X_2^2 + 35.28D_{\text{hex}}^3X_2^3)} \end{cases}, \quad (\text{C10})$$

where $X_1 = \theta(s)$, $X_2 = \theta'(s)$, and we assume $v = 0$.

We use ODE45 in MATLAB to numerically solve Eq. (C10). Since the solving algorithm only takes into account the initial conditions, we specifically use the boundary condition at the free end ($s = L$) to solve the governing equations. Based on the experimental observations of the nanocantilevers deformations (e.g., Fig. 4), we measure the rotation angle at the free end using the Canny method. The obtained angles at the free end are then used as one of the boundary conditions (i.e., $X_1(L) = \theta|_{s=L}$), while the other boundary condition is: $X_2(L) = \theta'|_{s=L} = 0$.

Figure 10 provides the deformation shapes of the nanocantilevers for different hexagonal diameters D_{hex} and rib widths W_{rib} solved by the nonlinear governing equations in Eq. (C9). Note that Fig. 10 leads to the 3D theoretical results presented in Fig. 4. Table II gives the external forces used to solve the governing equation.

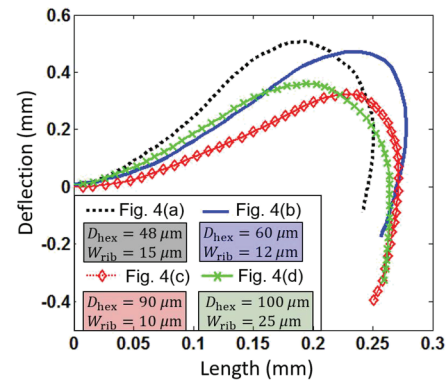


FIG. 10. Deformation shapes between the nanocantilevers with different hexagonal diameters and rib widths. ($t = 25$ nm for all cases).

TABLE II. External forces in the governing equation.

	Rotation angle at free end (°)	N_x (nN)	N_y (nN)
Fig. 4(a)	-60	-6.5	9.5
Fig. 4(b)	-55	-7.5	10
Fig. 4(c)	-75	5.5	7
Fig. 4(d)	-80	6	6.5

APPENDIX D: VALIDATION OF THE THEORETICAL MODEL

Figure 11 presents the deflection differences between the theoretical, numerical, and experimental results presented in Fig. 4. The Canny edge method is used to obtain the deflection-length curves of the FE and experimental results and then compared with the theoretical results in Fig. 10. The nanocantilevers are discretized into 19 segments with a total of $i = 20$ nodes, and thus we have

$$\begin{cases} \text{Diff}_{\text{Exp vs Num}, i} = \frac{|Y_{\text{Exp},i} - Y_{\text{Num},i}|}{Y_{\text{Exp},i}} \times 100 (\%) \\ \text{Diff}_{\text{Exp vs Theo}, i} = \frac{|Y_{\text{Exp},i} - Y_{\text{Theo},i}|}{Y_{\text{Exp},i}} \times 100 (\%) \end{cases}, \quad (\text{D1})$$

where Y_{Exp} , Y_{Num} , and Y_{Theo} are the deflections obtained from the experimental, numerical, and theoretical results, respectively.

We can see from Fig. 11 that the maximum differences for all four cases in Fig. 4 are less than 10%, which demonstrates the accuracy of the reported theoretical and numerical models.

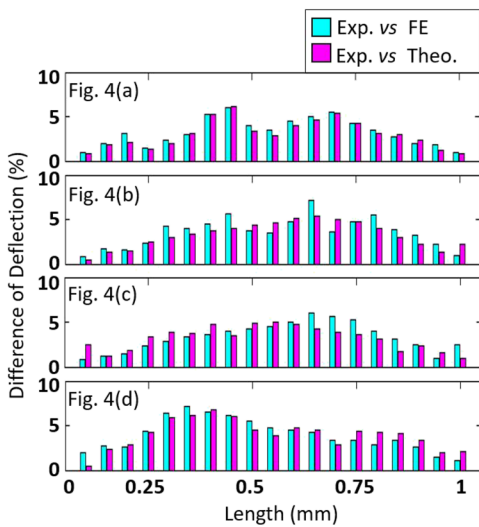


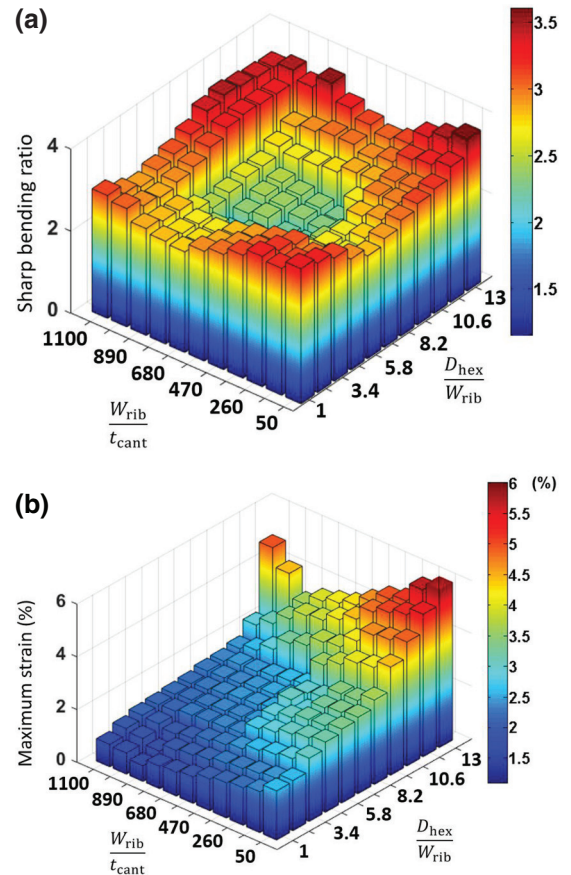
FIG. 11. Differences of the deformation shapes in Fig. 4 between the experimental, numerical, and theoretical results.

APPENDIX E: FE RESULTS FOR PARAMETRIC STUDIES

To investigate the effect of the geometries, that is, thickness t , hexagonal diameter D_{hex} , and rib width W_{rib} , on the mechanical response of the nanocantilevers, we define the sharp bending ratio and maximum principal strains with respect to the ratios of hexagonal diameter-to-rib width $D_{\text{hex}}/W_{\text{rib}}$ and rib width-to-thickness W_{rib}/t . Figure 12 presents the discrete (nonfitted) sharp bending ratio and maximum principal strain of the plate mechanical meta-materials obtained using the numerical models. Note that Fig. 12 leads to Fig. 5.

APPENDIX F: DESIGN CRITERIA AND VIOLATIONS OF THE CORRUGATED PATTERNS

Two design criteria are implemented to obtain the honeycomb corrugation pattern: (1) the no-straight-line rule (i.e., no straight lines can go through the corrugated plates without contacting sidewalls); and (2) the regularity rule (i.e., uniform pattern cells are separated by a uniform gap).


 FIG. 12. (a) Sharp bending ratio and (b) maximum principal strain of the nanocantilevers with respect to $D_{\text{hex}}/W_{\text{rib}}$ and W_{rib}/t .

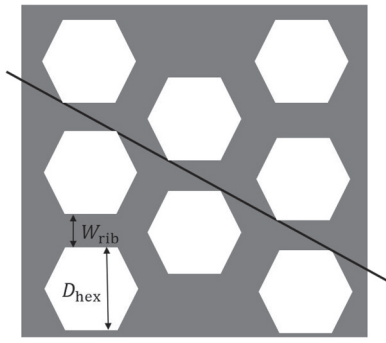


FIG. 13. Criterion of the no-straight-line rule for the nanocantilevers with hexagonal corrugation.

The no-straight-line rule is defined since straight lines allow the formation of wrinkles, which severely reduce the bending stiffness of the nanostructures and make them nonreproducible. The geometric limit that satisfies the no-straight-line rule in the corrugated hexagon nanocantilever is obtained as

$$D_{hex} \geq 3W_{rib}. \tag{F1}$$

The regularity rule is defined since there can be numerous arbitrary designs that satisfy the no-straight-line rule, but can be difficult to implement in practice.

Figure 13 displays the violation of the no-straight-line rule. When the hexagonal pattern of the nanocantilevers breaks the straight-line limit defined in Eq. (F1), the deformation resistance (i.e., bending stiffness) of the nanostructures is severely reduced. Consequently, the nanocantilevers are nonreproducible.

APPENDIX G: COMPARISON OF SHARP BENDING RATIO AND RECOVERY BETWEEN HEXAGONAL, RHOMBILLE AND BASKETWEAVE PATTERNS

Figure 14 presents the density plots of the recoverably sharp bending for the (a) rhombille and (b) basketweave nanocantilevers. The phenomena of sharp bending with full recovery are obtained from both architected cantilevers. However, the honeycomb corrugation gives the best performance of recoverable sharp bending (i.e., the largest overlap).

APPENDIX H: VIDEOS OF COMPARISON BETWEEN EXPERIMENTAL AND NUMERICAL DEFORMATION PROFILES

Videos 1 and 2 compare the experimental and numerical deformation profiles of the cantilevered nanocantilevers throughout the loading and unloading processes. It can be

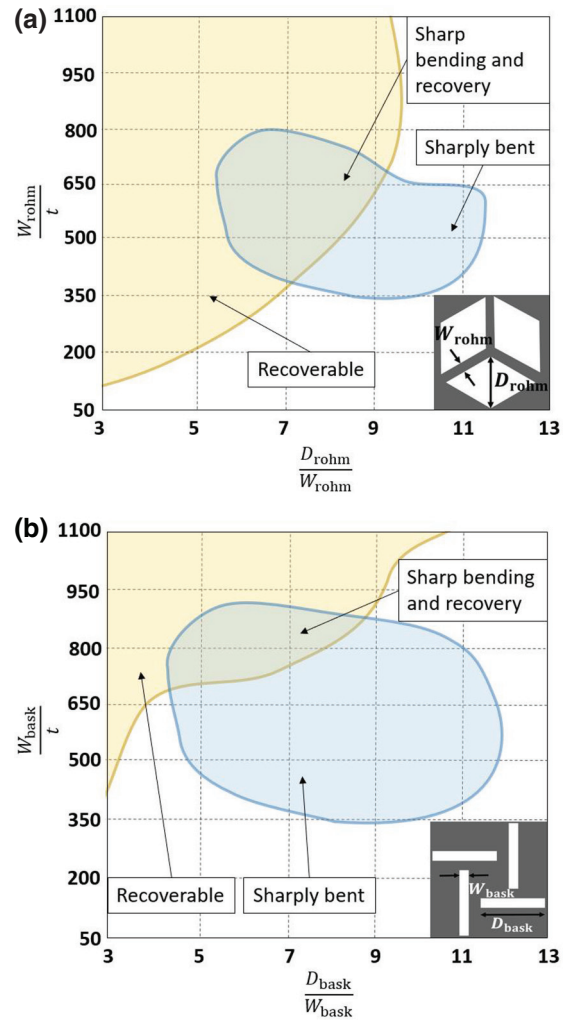
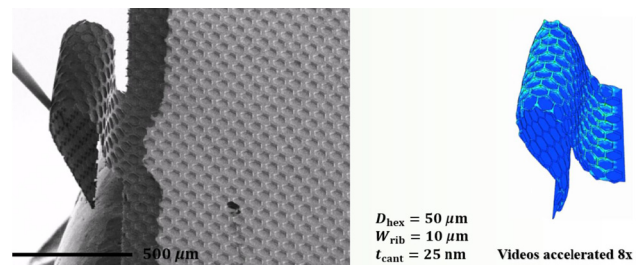
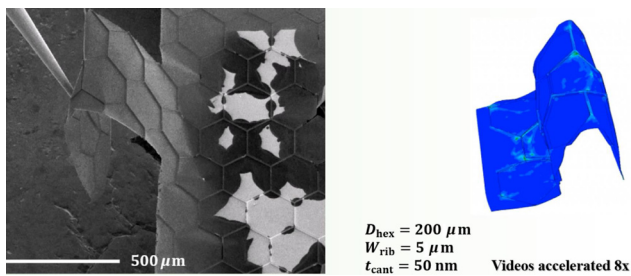


FIG. 14. Density plots for the sharp bending and recovery of the nanocantilevers with (a) rhombille pattern and (b) basketweave pattern.

seen that excellent agreements are obtained from nanocantilevers with different geometries.



VIDEO 1. Comparison of the experimental and numerical deformation profiles of the nanocantilever throughout the loading and unloading processes ($D_{hex} = 50 \mu\text{m}$, $W_{rib} = 10 \mu\text{m}$, and $t_{cant} = 25 \text{nm}$).



VIDEO 2. Comparison of the experimental and numerical deformation profiles of the nanocantilever throughout the loading and unloading processes ($D_{\text{hex}} = 200 \mu\text{m}$, $W_{\text{rib}} = 5 \mu\text{m}$, and $t_{\text{cant}} = 50 \text{nm}$).

- [1] M. Ben Amar and Y. Pomeau, Crumpled paper, *Proc. R. Soc. A* **453**, 729 (1997).
- [2] S. Conti and F. Maggi, Confining thin elastic sheets and folding paper, *Arch. Ration. Mech. Anal.* **187**, 1 (2008).
- [3] C. T. Orłowski and A. R. Girard, Modeling and simulation of nonlinear dynamics of flapping wing micro air vehicles, *AIAA J.* **49**, 969 (2011).
- [4] D. J. Pines and F. Bohorquez, Challenges facing future micro-air-vehicle development, *J. Aircraft* **43**, 290 (2006).
- [5] A. M. Mountcastle, E. F. Helbling, and R. J. Wood, An insect-inspired collapsible wing hinge dampens collision-induced body rotation rates in a microrobot, *J. R. Soc. Interface* **16**, 20180618 (2018).
- [6] K. Jensen, W. Mickelson, A. Kis, and A. Zettl, Buckling and kinking force measurements on individual multiwalled carbon nanotubes, *Phys. Rev. B* **76**, 195436 (2007).
- [7] M. Kadic, T. Buckmann, N. Stenger, M. Thiel, and M. Wegener, On the practicability of pentamode mechanical metamaterials, *Appl. Phys. Lett.* **100**, 191901 (2012).
- [8] A. A. Zadpoor, Mechanical meta-materials, *Mater. Horiz.* **3**, 371 (2016).
- [9] C. Coullais, C. Kettens, and M. van Hecke, A characteristic length scale causes anomalous size effects and boundary programmability in mechanical metamaterials, *Nat. Phys.* **14**, 40 (2018).
- [10] A. S. Meeussen, J. Paulose, and V. Vitelli, Geared Topological Metamaterials with Tunable Mechanical Stability, *Phys. Rev. X* **6**, 041029 (2016).
- [11] S. C. Han, J. W. Lee, and K. Kang, A new type of low density material: Shellular, *Adv. Mater.* **27**, 5506 (2015).
- [12] W. Lee, D. Y. Kang, J. Song, J. H. Moon, and D. Kim, Controlled unusual stiffness of mechanical metamaterials, *Sci. Rep.* **6**, 20312 (2016).
- [13] M. J. Mirzaali, R. Hedayati, P. Vena, L. Vergani, M. Strano, and A. A. Zadpoor, Rational design of soft mechanical metamaterials: Independent tailoring of elastic properties with randomness, *Appl. Phys. Lett.* **111**, 051903 (2017).
- [14] J. Bauer, J. R. Meza, T. A. Schaedler, R. Schwaiger, X. Zheng, and L. Valdevit, Nanolattices: An emerging class of mechanical metamaterials, *Adv. Mater.* **29**, 1701850 (2017).
- [15] S. Janbaz, M. McGuinness, and A. A. Zadpoor, Multimaterial Control of Instability in Soft Mechanical Metamaterials, *Phys. Rev. Appl.* **9**, 064013 (2018).
- [16] A. Rafsanjani, A. Akbarzadeh, and D. Pasini, Snapping mechanical metamaterials under tension, *Adv. Mater.* **27**, 5931 (2015).
- [17] T. Frenzel, M. Kadic, and M. Wegener, Three-dimensional mechanical metamaterials with a twist, *Science* **358**, 1072 (2017).
- [18] L. R. Meza, S. Das, and J. R. Greer, Strong, lightweight, and recoverable three-dimensional ceramic nanolattices, *Science* **345**, 1322 (2014).
- [19] X. Zheng, H. Lee, T. H. Weisgraber, M. Shusteff, J. DeOtte, E. B. Duoss, J. D. Kuntz, M. M. Biener, Q. Ge, J. A. Jackson, S. O. Kucheyev, N. X. Fang, and C. M. Spadaccini, Ultralight, ultrastiff, mechanical metamaterials, *Science* **344**, 1373 (2014).
- [20] J. H. Pikul, Z. Dai, X. Yu, H. Zhang, T. Kim, P. V. Braun, and W. P. King, Micromechanical devices with controllable stiffness fabricated from regular 3D porous materials, *J. Micromech. Microeng.* **24**, 105006 (2014).
- [21] K. A. Seffen, Mechanical memory metal: A novel material for developing morphing engineering structures, *Scr. Mater.* **55**, 411 (2006).
- [22] K. A. Seffen, Hierarchical multi-scale shapes in mechanical memory metal, *Scr. Mater.* **56**, 417 (2007).
- [23] K. Davami, L. Zhao, E. Lu, J. Cortes, C. Lin, D. E. Lilley, P. K. Purohit, and I. Bargatin, Ultralight shape-recovering plate mechanical metamaterials, *Nat. Commun.* **6**, 10019 (2015).
- [24] C. Lin, S. M. Nicaise, D. E. Lilley, J. Cortes, P. Jiao, J. Singh, M. Azadi, G. G. Lopez, M. Metzler, P. K. Purohit, and I. Bargatin, Nanocardboard as a nanoscale analog of hollow sandwich plates, *Nat. Commun.* **9**, 4442 (2018).
- [25] Abaqus/CAE User's Manual. SIMULIA (2016). Available at: <http://130.149.89.49:2080/v2016/index.html>.
- [26] Q. Xu, S. Varadarajan, C. Chakrabarti, and L. J. Karam, A distributed canny edge detector: Algorithm and FPGA implementation, *IEEE Trans. Image Process.* **23**, 2944 (2014).
- [27] L. G. Barzler, On the flexure of thin cylindrical shells and other "thin" sections, *Proc. R. Soc. A* **116**, 104 (1927).
- [28] B. Audoly and Y. Pomeau, *Elasticity and Geometry: From Hair Curls to the Non-Linear Response of Shells* (Oxford University Press, Oxford, England, UK, 2010).
- [29] R. D. James, The equilibrium and post-buckling behavior of an elastic curve governed by a non-convex energy, *J. Elast.* **11**, 239 (1981).
- [30] J. W. Hutchinson and K. W. Neale, Neck propagation, *J. Mech. Phys. Solids* **31**, 406 (1983).
- [31] J. L. Ericksen, *Introduction to the Thermodynamics of Solids* (Springer, New York City, New York, US, 1998), ISBN-10: 9780727726339.
- [32] L. Jin, A. Takei, and J. W. Hutchinson, Mechanics of wrinkle/ridge transitions in thin film/substrate systems, *J. Mech. Phys. Solids* **81**, 22 (2015).
- [33] B. T. Berg, Bending of superelastic wires, part I: Experimental aspects, *J. Appl. Mech.* **62**, 459 (1995).

- [34] R. L. Fosdick and R. D. James, The elastic and the problem of the pure bending for a non-convex stored energy function, *J. Elast.* **11**, 165 (1981).
- [35] M. Arroyo and T. Belytschko, Nonlinear Mechanical Response and Rippling of Thick Multiwalled Carbon Nanotubes, *Phys. Rev. Lett.* **91**, 215505 (2003).
- [36] N. J. Bechle and S. Kyriakides, Localization in NiTi tubes under bending, *Int. J. Solids Struct.* **51**, 967 (2014).
- [37] M. B. Rubin, *Cosserate Theories: Shells, Rods and Points* (Springer, New York City, New York, US, 2000). ASIN: B01FKSAK2E.
- [38] S. H. Jen, J. A. Bertrand, and S. M. George, Critical tensile and compressive strains for cracking of Al_2O_3 films grown by atomic layer deposition, *J. Appl. Phys.* **109**, 084305 (2011).
- [39] B. F. Tatting, Z. Gurdal, and V. V. Vasiliev, The Brazier effect for finite length composite cylinders under bending, *Int. J. Solids Struct.* **34**, 1419 (1997).
- [40] Y. Chen, A. Ong, and R. J. Wood, An efficient method for the design and fabrication of 2D laminate robotic structures, *IEEE Int. Conf. Real-time Comput. Robot.* (2018), pp. 1–6.
- [41] B. Singh and I. Chopra, Insect-based hover-capable flapping wings for micro air vehicles: Experiments and analysis, *AIAA J.* **46**, 2115 (2008).
- [42] Y. Jiang, L. M. Korpas, and J. R. Raney, Bifurcation-based embodied logic and autonomous actuation, *Nat. Commun.* **10**, 128 (2019).
- [43] P. Jiao, W. Borchani, H. Hasni, and N. Lajnef, Enhancement of quasi-static strain energy harvesters using non-uniform cross-section post-buckled beams, *Smart Mater. Struct.* **26**, 085045 (2017).
- [44] W. Borchani, P. Jiao, R. Burgueno, and N. Lajnef, Control of postbuckling mode transitions using assemblies of axially loaded bilaterally constrained beams, *J. Eng. Mech.* **143**, 04017116.
- [45] H. A. Atwater, A. R. Davoyan, O. Ilic, D. Jarwala, M. C. Sherrott, C. M. Went, W. S. Whitney, and J. Wong, Materials challenges for the Startshot lightsail, *Nat. Mater.* **17**, 861 (2018).
- [46] See Supplemental Material at <http://link.aps.org/supplemental/10.1103/PhysRevApplied.11.034055> for detailed discussions on the fabrication and numerical modelling of nanoplates, and nonlinearly fitting of the nonmonotonic moment-curvature relation.